Available online at www.sciencedirect.com
SCIENCE DIRECT®
ELSEVIER
Nuclear Instruments and Methods in Physics Research A 515 (2003) 497–523
NUCLEAR INSTRUMENTS & METHODS IN PHYSICS RESEARCH Section A
www.elsevier.com/locate/nima

FIASCO: a multidetector optimized for semiperipheral heavy ion collisions at Fermi energies

M. Bini, G. Casini, A. Olmi*, G. Poggi, A.A. Stefanini, L. Bardelli, A. Bartoli, L. Bidini, C. Coppi, P. Del Carmine, A. Mangiarotti, P.R. Maurenzig, G. Pasquali, S. Piantelli, S. Poggi, N. Taccetti, E. Vanzi

Dipartimento di Fisica dell'Università and Sezione INFN di Firenze, Via G. Sansone 1, Sesto Fiorentino, Italy

Received 3 March 2003; received in revised form 27 June 2003; accepted 1 July 2003

Abstract

The FIASCO multidetector is a low-threshold apparatus, optimized for the investigation of peripheral to semi-central collisions in heavy ion reactions at Fermi energies. It consists of three types of detectors. The first detector layer is a shell of 24 position-sensitive Parallel Plate Avalanche Detectors (PPADs), covering about 70% of the forward hemisphere, which measure the velocity vectors of the heavy ($Z \gtrsim 10$) reaction products. Below and around the grazing angle, behind the most forward PPADs, there are 96 ΔE–E silicon telescopes (with thickness of 200 and 500 μm, respectively); they are mainly used to measure the energy of the projectile-like fragment and to identify its charge and, via the time-of-flight of the PPADs, also its mass. Finally, behind most of the PPADs there are 158 (or 182, depending on the configuration) scintillation detectors, mostly of the phoswich type, which cover 25–30% of the forward hemisphere; they identify both light charged particles ($Z = 1, 2$) and intermediate mass fragments ($3 \leqslant Z \lesssim 20$), measuring also their time-of-flight.

PACS: 25.70. − z; 29.40. − n; 29.40.Cs; 29.40.Mc; 29.40.Wk; 07.05.Hd

Keywords: Heavy ion collisions; Multifragment emission; Multidetector system; Position sensitive gas detectors; Silicon detectors; Phoswich detectors; Data acquisition

1. Introduction

The FIASCO[1] multidetector (Florentine Initiative After Superconducting Cyclotron Opening) was

*Corresponding author.
E-mail addresses: olmi@fi.infn.it (A. Olmi), poggi@fi.infn.it (G. Poggi).

[1] In Italian language, "*fiasco*" is the long-necked straw-covered rounded bottle, traditionally used for Chianti, Tuscany's most famous wine. It dates back to 1200, its form having origin in vessels used in Greek and Roman banquets. FIASCO has a similar shape (see Fig. 4), with its bulbous body (the detectors around the target) and the long neck ending in a big cork (the detectors with long flight-paths at very forward angles). We hope that the widespread and more recent meaning of "complete failure", "big unsuccess" (possibly coming from Venetian glassblowers who turned any hand-crafted fine-blown glassware with the slightest flaw into a simple utilitarian flask) has nothing to do with our apparatus.

0168-9002/$ - see front matter © 2003 Elsevier B.V. All rights reserved.
doi:10.1016/j.nima.2003.07.064

specifically designed and built by the Heavy Ion Group of the INFN and the Department of Physics of the University of Florence for studying non-central collisions in heavy ion reactions at Fermi energies (i.e. at bombarding energies between 15 and 40 AMeV) with the beams delivered by the Superconducting Cyclotron of the Laboratori Nazionali del Sud (LNS) of INFN in Catania (Italy).

It is well known that in this energy region the major fraction of the cross section for non-central collisions consists of quasi binary events, with two heavy fragments in the exit channel, the projectile residue being strongly focused in the forward direction. The possible presence of three (or four) heavy fragments in the exit channel has been ascribed mainly to the sequential fission of one (or both) of the colliding partners [1]. With increasing bombarding energy the binary character of the reaction mechanism is increasingly perturbed, even for peripheral collisions, by the occurrence of dynamical effects, like prompt midvelocity emission of Light Charged Particles (LCPs) and Intermediate Mass Fragments (IMFs) [2–8].

In such a scenario, in order to carry out a good event reconstruction of the peripheral collisions, it is necessary to measure not only the projectile-like fragment (PLF), but also the target-like fragment (TLF); for this purpose low thresholds for the detection of heavy ($Z \gtrsim 10$) fragments are required, because of the very low recoil energy of the TLF. The apparatus is thus equipped with 24 position-sensitive Parallel Plate Avalanche Detectors (PPADs), covering a solid angle of about 70% of the forward hemisphere. Their very low thresholds (≈ 0.1 AMeV) together with the use of a thin target (of the order of a few 100 $\mu g/cm^2$) allow one to reconstruct the complete kinematics of the event (by means of the Kinematic Coincidence Method, KCM [9]) even for small inelasticities, up to the elastic collisions. This property differentiates the FIASCO setup with respect to almost all other multidetectors presently in use, which generally identify only the projectile residue (see, for example, Ref. [10]). By virtue of the detection of both PLF and TLF, the KCM gives a way to estimate the centrality of the collision by means of the Total Kinetic Energy Loss, i.e. by the amount of kinetic energy lost with respect to the entrance channel.

In order to put in evidence the existence of non-equilibrium effects in the evaporation chain of heavy projectile-like fragments [11,12], 96 silicon telescopes ΔE–E are used to identify the fragment atomic number Z and to measure its kinetic energy. The aim is to determine the secondary (i.e. post-evaporative) charge of the projectile residue and to extract its secondary mass by means of the time of flight measured in coincidence by the PPADs.

The complete characterization of the event requires also the detection of the lighter reaction products. Therefore a good sampling of the forward hemisphere (25–30%) is obtained by means of scintillation detectors (158 phoswich telescopes, or 154 phoswiches plus 28 CsI(Tl), depending on the configuration), located behind almost all the PPADs, for the identification of LCPs ($Z = 1, 2$) and IMFs ($3 \leqslant Z \lesssim 20$) and the measurement of their time-of-flight. The choice of the phoswich telescopes for the detection of LCPs and IMFs has been partly dictated by their relatively low cost, since it was necessary to obtain a quite large coverage.

The FIASCO setup was used in two different measurement campaigns. The first one was performed in December 1998–January 1999 for the system $^{93}Nb + ^{116}Sn$ at 29.5 AMeV in direct and reverse kinematics; the second one was performed between February and July 2001, for the same systems at bombarding energies of 17, 23, 30 and 38 AMeV. In the second campaign the phoswich telescopes behind one of the PPADs located at polar angle between 20° and 60° were replaced by the hodoscope HODO-CT[2] of the TEMPERATURE experiment [13].

[2] HODO-CT is an array of 96 3-layer telescopes, each of them with a 3×3 cm^2-wide active area, consisting of a 50 μm silicon ΔE detector, followed by a 300 μm-thick silicon ΔE_2 detector and by a 6 cm-thick CsI(Tl) scintillator (E detector) read-out by a photodiode; the detectors were placed 60 cm far from the target position on a spherical surface, covering a total solid angle of 230 mstr.

2. Mechanical assembly

The FIASCO experimental setup was mounted inside the CICLOPE scattering chamber of LNS, a large-volume ($\sim 70\ m^3$) multipurpose vacuum vessel with a $5\ m \times 2.5\ m$ platform for the installation of big detector systems. Fig. 1 shows two views of the apparatus in the working position inside the scattering chamber, as it was assembled in the first campaign. The mechanical support of the detectors consists of 5 steel rings (#1–5), shaped as regular octagons with inner diameter of about 160 cm, mounted downstream with respect to the target, at distances which can be varied by sliding the rings on two rails (see Figs. 1 and 2).

All the detectors are arranged in 26 detector blocks (#1–26). A typical block consists of one PPAD followed by an array of phoswich detectors (Fig. 3, lower part); however, the last 2 blocks (#25–26), placed at backward angles, have only phoswiches, without PPADs in front. The first six blocks (#1–6), located at small angles, include also 16 silicon telescopes each, which are mounted in between the PPADs and the phoswiches (or, in the second campaign, CsI crystals, see Fig. 3, upper part).

The PPADs are mounted on 24 supporting frames, connected to the octagonal rings with rods held by clamps (see Fig. 2). The PPADs are numbered from #1 to #24 starting from the most forward ring (ring #1). The position of the PPADs in the first campaign is shown in Fig. 4 (side view) and Fig. 5 (polar representation). The adopted reference frame is a right-hand polar frame, centered on the target position, with the polar axis pointing downstream along the beam axis: ϑ and φ are the polar and azimuthal angles, respectively.

In the first campaign only 20 out of the 24 frames were equipped with a box housing the

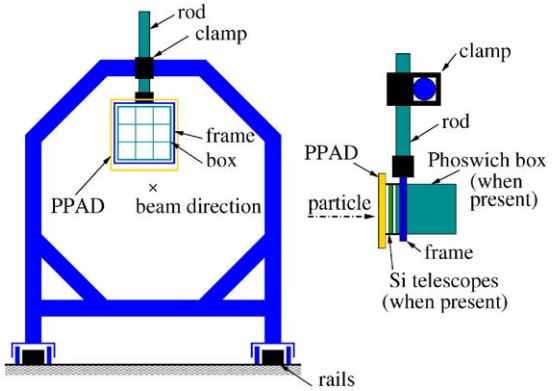

Fig. 2. The sketch of a ring as viewed from the target (left part) and side view of the mechanical assembly of one detector module (right part).

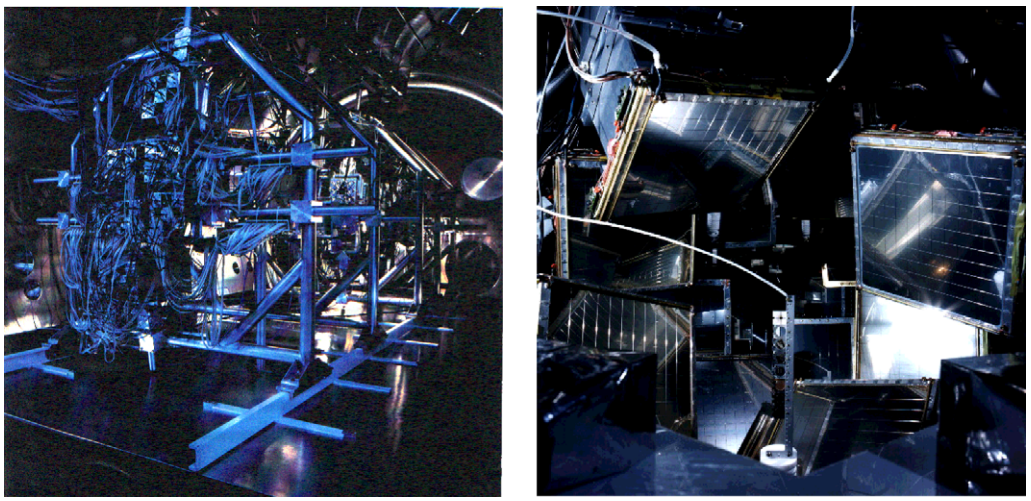

Fig. 1. Photograph of the experimental apparatus mounted inside the CICLOPE scattering chamber during the first campaign. Left side: view from the rear side of the most forward ring (#1). Right side: view of the target region from upstream.

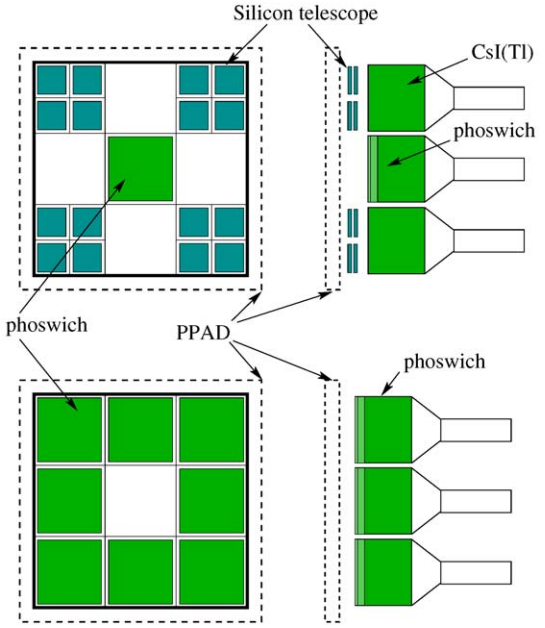

Fig. 3. Upper part: blocks #1–6, front (on the left) and side view (on the right), with the PPAD removed. Lower part: blocks #7–24, front (on the left) and side view (on the right), with the PPAD removed.

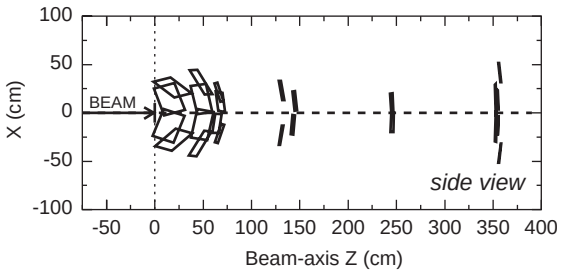

Fig. 4. Schematic drawing of the experimental setup (side view) in the first campaign. The long flight path for the PLF fragments is apparent (distance of most forward detectors from the target ≈ 3.5 m).

scintillation detectors, which were all of the phoswich type; Table 1 lists the geometrical position of all the detectors and their subtended solid angles. In the second campaign all the PPADs but one (that in front of the hodoscope) had their box for the scintillators. The arrangement of the detectors was similar to that of the first campaign, the main differences being that:

(1) the phoswiches behind the silicon telescopes of the forward PPADs (#1–6) were replaced with 24 CsI(Tl) scintillators;
(2) the phoswiches behind the PPAD #18 were replaced with the hodoscope HODO-CT [13];
(3) all the phoswiches made available with these replacements were used to fill the boxes behind PPADs #9, 11, 14 and 16, which were absent in the first campaign.

The boxes housing the phoswiches are divided into 3×3 cells and can thus carry up to a maximum of nine detectors. In the actual setup, these boxes contain five (blocks #1–6) or eight (blocks #7–24) phoswich telescopes (see Figs. 3 and 6). Moreover, the 16 phoswich telescopes at the most backward angles (blocks #25, 26) are not housed in boxes, but simply placed on a table lying in a horizontal plane at about beam height. The 16 ΔE–E silicon telescopes behind each of the 6 most forward PPADs are mounted, in groups of 4, in front of the scintillation detectors at the four corners of the box (see Fig. 3).

Finally, a beam-monitor, made of a fast plastic scintillator (BC404) coupled to a fast photomultiplier, is mounted in an empty position of box #2. Being located below the grazing angle for all the studied reactions, it is used to detect the elastically scattered projectiles and to monitor the time structure of the beam.

In our experiments we use a motorized target holder, with a ladder carrying several targets, so that they can be changed without breaking the vacuum. A high voltage of up to +40 kV has been always applied to the insulated target ladder, in order to strongly suppress the background of electrons ejected from the target at the passage of the beam particles.

2.1. Measurement of the setup geometry

In order to have a precise measurement of the velocity vectors, great importance has been given to the development of a procedure which: (a) allows for an accurate measurement of the geometry of the experimental setup; (b) reduces risky operations in the vicinity of the very delicate gas detectors and (c) does not require access to the

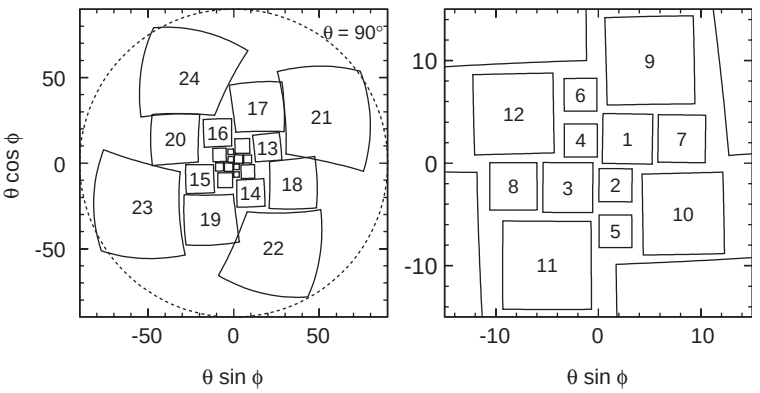

Fig. 5. Active area of the gas detectors in polar representation (front view) during the first campaign. On the left total view; on the right detail of the most forward gas detectors mounted around the beam axis at (0,0).

Table 1
Geometry and solid angles of the detectors in the first campaign. The first and the second columns give the ring number and the detector block number, respectively. *Dist*, ϑ_0 and φ_0 refer to the center of each PPAD (or of the blocks #25, 26). For each block, $\Delta\Omega$, $\Delta\Omega_s$ and $\Delta\Omega_p$ are the solid angles subtended by the PPAD and by the following n_s silicon telescopes and n_p phoswiches, respectively

Position		PPAD				Silicon		Phoswich	
Ring #	Block #	Dist (mm)	ϑ_0 (deg)	φ_0 (deg)	$\Delta\Omega$ (mstr)	n_s	$\Delta\Omega_s$ (mstr)	n_p	$\Delta\Omega_p$ (mstr)
1	1	3533	3.7	50.1	7.2	16	1.0	5	1.6
	2	3556	2.7	142.2	3.2	16	1.0	5	1.6
	3	3534	3.8	−128.7	7.2	16	1.0	5	1.6
	4	3554	2.8	−37.8	3.2	16	1.0	5	1.6
	5	3596	6.8	165.9	3.1	16	1.0	5	1.6
	6	3594	6.9	−14.7	3.1	16	1.0	5	1.6
2	7	2478	8.5	73.7	6.5	—	—	8	5.3
	8	2484	8.6	−105.3	6.5	—	—	8	5.3
3	9	1337	11.2	26.7	22	—	—	—	—
	10	1448	9.6	120.8	19	—	—	8	15.6
	11	1331	11.2	−153.3	23	—	—	—	—
	12	1468	9.6	−59.9	19	—	—	8	15.2
4	13	730	21.8	64.7	75	—	—	8	61.5
	14	712	20.1	150.4	79	—	—	—	—
	15	694	21.9	−114.9	83	—	—	8	68.0
	16	706	20.1	−27.9	80	—	—	—	—
	17	590	36.0	23.5	259	—	—	8	94.1
	18	615	37.0	109.2	238	—	—	8	86.6
	19	582	36.1	−157.7	266	—	—	8	96.7
	20	610	37.6	−67.6	242	—	—	8	88.1
5	21	332	63.6	61.8	817	—	—	8	297
	22	355	57.2	155.8	714	—	—	8	260
	23	331	64.7	−116.1	821	—	—	8	299
	24	344	58.4	−27.4	761	—	—	8	277
–	25	423	100–170	90	—	—	—	8	183
–	26	417	100–170	−90	—	—	—	8	188

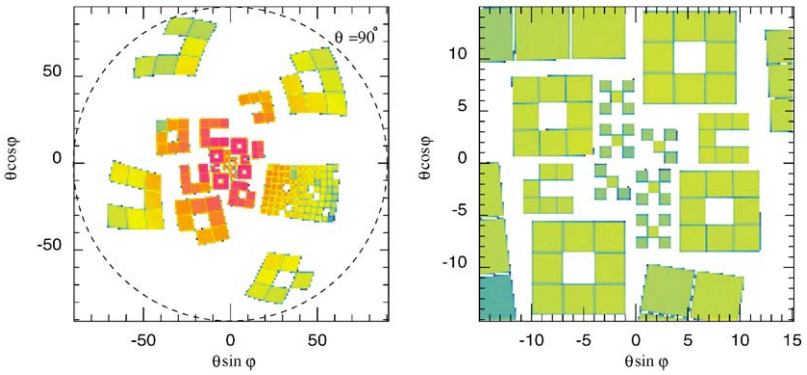

Fig. 6. Polar representation of the experimental yield collected by the phoswich telescopes and by the hodoscope HODO-CT for the $^{93}Nb + ^{116}Sn$ reactions at 30 AMeV in the second campaign (a few detectors which did not work properly are missing). On the left: total view of the forward hemisphere; on the right: detail of the zone at small polar angles. For each detector, the counts have been randomly distributed on its surface.

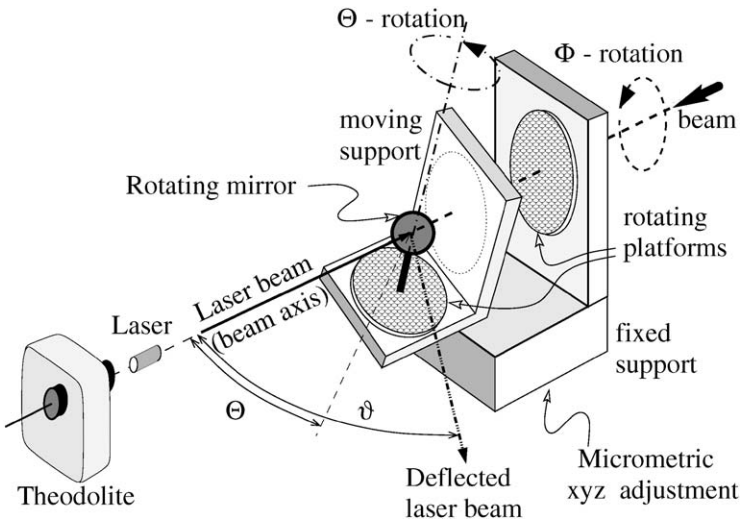

Fig. 7. Sketch of the mechanical assembly for measuring the setup geometry.

very detector-crowded region around the target. This has been done by temporarily replacing the target-holder with the mechanical assembly shown in Fig. 7. It basically consists of a mirror mounted on a two-angle precision goniometer, realized by means of two rotating platforms, driven by step motors. The first platform, which rotates around the beam axis, is mounted on a fixed support, firmly connected to the target "pivot". The second one, whose rotation axis is perpendicular to the beam axis, lies on a moving support (mounted on the first platform) and holds the mirror.

A Nikon Total Station (theodolite with electronic distance measurement) and a small solid-state laser are mounted coaxially at the exit of the scattering chamber. The laser is small enough to fully maintain the distance measurement functionality of the Nikon device. The laser and the theodolite are aligned with the beam axis and point to the rotating mirror at the target position, while four reflectors are mounted on the four corners of the front face of each PPAD. By proper rotation of the mirror, the reflected laser beam is aimed at the reflectors on a selected PPAD: the

rotation angle Φ of the first platform gives directly the azimuthal angle φ of the reflector aimed at, while the rotation angle of the second platform, Θ, is just half of its polar angle ϑ with respect to the beam axis.

The electronic distance measurement method is the standard one, using the interference of the modulated infrared light emitted by the Total Station and that reflected back by the object aimed at. In our application, the infrared light follows exactly the same path as the beam of the small coaxial laser. Therefore the obtained distance is the sum of that from the Total Station to the mirror plus that from the mirror to the considered reflector. The distances between the target and the various reflectors are then obtained by subtracting the common mirror-Total Station distance; the latter is determined once and for all by orienting the mirror perpendicularly, so that the infrared light is directly reflected back into the Total Station.

In this way, from the measured distances and angles of the reflectors it is possible to obtain the distance and angular position of the associated PPAD (as well as those of the phoswiches and silicon telescopes behind it, as their relative position with respect to the PPAD is known).

Special care has been devoted to reaching the accuracy needed for this measurements. First of all, the two platforms have been carefully assembled together so that the two rotation axes are coplanar and cross each other perpendicularly. Then, with the help of a second theodolite and via a set of micrometric rotation-, displacement- and tilting-devices, the fixed support has been positioned in such a way that the first rotation axis coincides with the beam axis and the second crosses the first one at the target position. Finally, other micrometric devices (not shown in Fig. 7), mounted on the second platform, have been used to position the mirror so that its reflecting surface is at the target position and contains the second rotation axis.

The nominal accuracy of the rotating platforms is $\pm 0.01^\circ$. Taking into account the alignment of the whole mechanical device, we estimate that the overall error on the angular measurements is well below $\pm 0.1^\circ$. For the measurement of the target–detector distances, the error is about ± 2 mm. This is the precision with which one knows the position of all gas detectors (and hence of all other detectors) with respect to the nominal beam axis and to the laboratory frame. However, for a good kinematic reconstruction of the reaction it is necessary to know also the alignment of the actual beam axis with the nominal one. During experiments, the beam is periodically focused onto the target center with the help of an alumina (Al_2O_3) plate mounted on the target ladder: the beam is steered until its luminescent spot almost disappears into a hole (of 2 mm radius) drilled in its center. The actual direction of the beam is roughly checked at run-time by periodically looking at its luminescent spot on a removable quartz plate located on the beam axis about 3 m downstream of the target.

In the off-line analysis, the actual alignment of the beam axis with respect to the nominal one can be checked with the elastic scattering data acquired in "singles". Assuming that the beam hits the target center, while its direction may slightly deviate from the nominal axis, the angular distributions of elastically scattered projectiles hitting the four most forward PPADs (in clean equal windows of the azimuthal angle φ) are simultaneously fitted with the Rutherford cross section, $\sigma_{\mathrm{Ruth}}(\vartheta_{\mathrm{lab}})$. The "best" correction to be applied to the data is determined by a χ^2 minimization with respect to a reference frame rotation. For all runs of the two campaigns, such a correction amounted to 0.2° at most (less than 8 mm in the plane of the most forward detectors).

3. The detectors

3.1. The gas detectors

3.1.1. Description

The Parallel Plate Avalanche Detectors (PPAD) are large-area position-sensitive gas detectors devoted to the detection of heavy fragments ($Z \gtrsim 10$) and to the determination of their velocity vectors. They measure the impact time of the impinging fragments and the impact position on two orthogonal coordinates, with only a rough

estimate of the energy deposited inside the detectors.

In the FIASCO setup two kinds of gas detectors, with very similar characteristics but different active area, are present: one type (called "*Quadro*") is about 30×30 cm^2 and the other (called "*Punto*") is about 20×20 cm^2. The *Quadro*'s were built some years ago in the "Detektor Labor" of GSI [14], Darmstadt, while the *Punto*'s have been recently designed and built in our laboratory in Florence. The 24 gas detectors of the FIASCO setup were 14 *Punto*'s and 10 *Quadro*'s in the first campaign and 16 *Punto*'s and 8 *Quadro*'s in the second one.

Both kinds of gas detectors have a central cathode made of a 1.5 μm thick double-side aluminized Mylar foil; on the opposite sides with respect to the cathode, two grids of anode wires are placed at a distance of 3 mm from the cathode, the wires of one grid being oriented perpendicular to those of the other one (see Fig. 8). These wires, made of gold-plated tungsten and with a diameter of 20 μm, are woven with a pitch of 1 mm. They are grouped two by two in the *Punto*'s and four by four in the *Quadro*'s and connected to lumped delay-line chains, one for the "x" coordinate and one for the "y" coordinate. The delay lines are made of passive DIP chips (with 3 ns taps and 50 Ω characteristic impedance) summing up to a total of 100(75) taps for the *Punto*'s (*Quadro*'s): they have been chosen of such a quality that the signal, while propagating along the lines, is attenuated less than a factor 2 for the whole

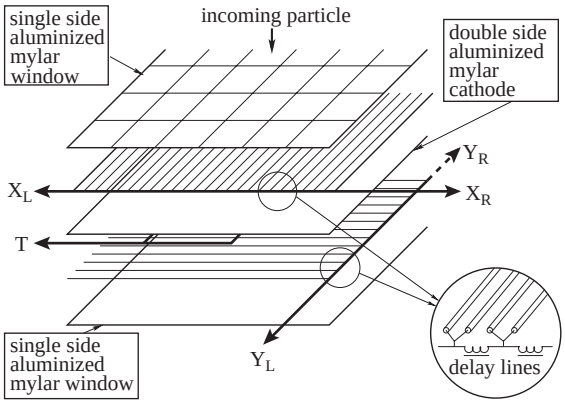

Fig. 8. The sketch of a gas detector.

chain. The gas volume of the *Quadro*'s (*Punto*'s) is delimited by two single-side aluminized Mylar windows with thickness of 1.5 μm (2 μm), corresponding to 0.21 (0.28) mg/cm^2. They provide the gas tightness of the detector, the leak rate of each of them being typically less than 1 mbar $\cdot\, \ell$/h. The gas volume, delimited by the windows, is filled with heptane (C_7H_{16}) at a pressure of about 3.5 mbar and a continuous gas flow (about 0.5 ℓ/min at 3.5 mbar) reduces the poisoning of the gas due both to molecular dissociation (caused by the irradiation) and to oxygen contamination (due to possible small leaks in the gas system outside the chamber). In order to be able to withstand the gas pressure with a limited deformation, the windows of each PPAD are supported by steel wires, 130 μm in diameter, forming meshes of 2 cm × 2 cm.

During operation, the cathode is kept at a voltage of about −500 V with respect to the anode wires. This corresponds to a working point in the proportional regime (reduced field equal to about 500 V cm^{-1} mbar^{-1}). A fragment penetrating the detector ionizes the gas along its track and an avalanche is produced due to the high electric field [15]. If the rate of impinging fragments is greater than about 1 kHz/cm^2, a permanent discharge may develop between the cathode and the anode wires. However, during the measurements the overall counting rate of each detector was kept lower than 100 kHz, well below the discharge limit.

The time mark is obtained from the cathode signal, while the impact point of the fragment is derived from the wire signals. Locally, the intrinsic time resolution of the PPADs is about 500 ps FWHM. However, due to their large area, the time of arrival of the cathode signals to the preamplifier depends on the impact point of the fragments on the detector, especially for the larger *Quadro* detectors. This position dependence may have several origins, like e.g. different development times of the avalanche (due to possible imperfections in the parallelism between cathode and wires) or different propagation times of the signal through the cathode. In order to reduce this position dependence of the time mark, the cathode signal is collected at two different points, at a

distance of about 10 cm from each other. Nevertheless, a residual dependence of the order of 1–2 ns still remains and a correction needs to be applied, in order to finally obtain an average time resolution (FWHM) of about 700 ps (for the elastic peak) over the whole detector area. This value is of the same order of the time resolution of the beam pulses, which in our experiments was between 600 ps and 1 ns (FWHM), depending on Cyclotron and beam optics tuning.

An example of the observed dependence of the time signal on the impact point is presented in Fig. 9 for one typical *Quadro*. The figure is obtained by dividing the active area of the detector in 100 square cells of $3\,\text{cm} \times 3\,\text{cm}$; in each cell the difference between the measured time-of-flight for elastic events and that calculated from the scattering angle is determined. Assuming that it does not appreciably depend on the energy and atomic number of the fragment, this difference is then used to correct the time mark of all fragments impinging on the considered detector cell. The lines in Fig. 9 show this time difference as a function of the "x" and "y" coordinates on the plane of the PPAD.[3] The charge integration of the cathode signal delivers also a rough information on the energy deposited inside the detector, with a resolution of about 30–40%.

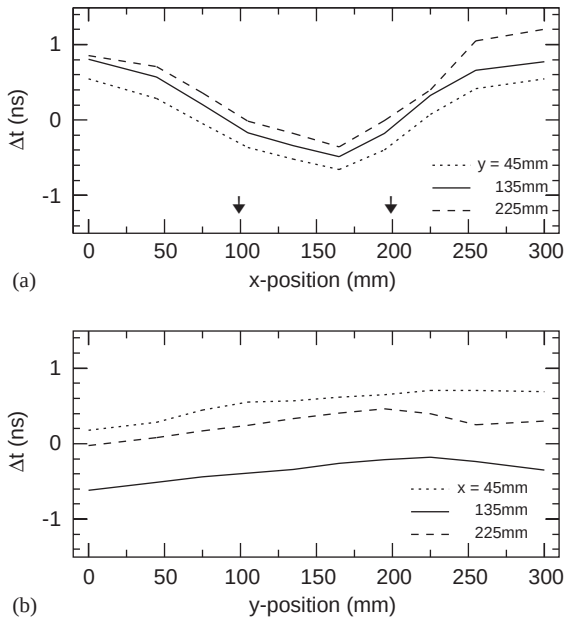

Fig. 9. Measured dependence of the time mark on the impact point for a gas detector (*Quadro* #1), presented as a function of one coordinate, "x" in (a) and "y" in (b), for three values of the other one. The arrows indicate the pick-up points at $y = 0$, $x = 100$ and 200 mm.

For each grid, the "position" signal induced by the gas avalanche on the nearest wires reaches the delay line and travels along it in both directions, until it is collected by preamplifiers at both ends; these two time marks carry information on the time-of-flight of the incoming particle plus the respective fraction of delay line traveled over. Which group of wires has fired in an event is usually deduced from the measured time difference between these time marks; the obtained spatial resolution is of the order of the distance between two groups of wires (about 2 and 4 mm FWHM). These two time marks (taking as zero the instant when the particle leaves the target) add up to twice the time-of-flight plus the fixed total delay of the line. This fact can be used to reject double hits in the PPADs, i.e. events in which two fragments impinge on the same detector and the time marks obtained at the ends of one delay line do not belong to the same fragment.

The PPADs have an efficiency of nearly 100% in a wide range of atomic number and energy. It is found that the experimentally measured efficiency can be empirically described by a Fermi-like distribution of velocity:

$$\varepsilon(v) = \frac{1}{\exp[(v - v_0(Z))/\sigma(Z)] + 1}$$

where v is the velocity of the detected ion and Z its atomic number. The empirically determined parameters v_0 and σ are found to vary with Z in an approximately linear way. Assuming such a linear dependence, a simultaneous fit with the above formula to the data of all the identified charges Z (from 8 to 15) has been performed for each detector. An example of the obtained results is shown in Fig. 10 where the efficiency of one PPAD is plotted as a function of the velocity v_{lab} for three

[3] For each PPAD a right-hand Cartesian frame of reference is used, with the origin in the farthest corner with respect to the beam axis and the z-axis directed from the detector toward the target.

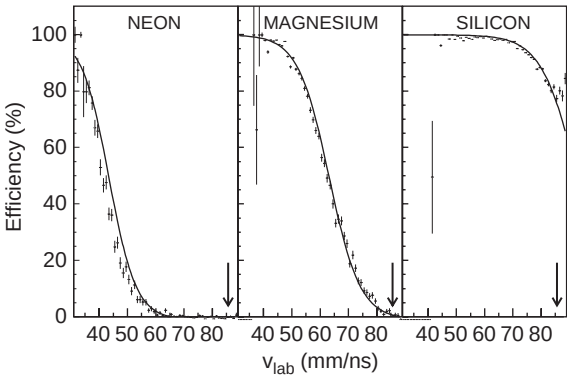

Fig. 10. Efficiency of a typical gas detector for three IMFs ($Z = 10,12,14$) as a function of their velocity. The arrows indicate the beam velocity for the reaction Nb + Nb at 38 AMeV. The continuous lines are the result of the fit (see text).

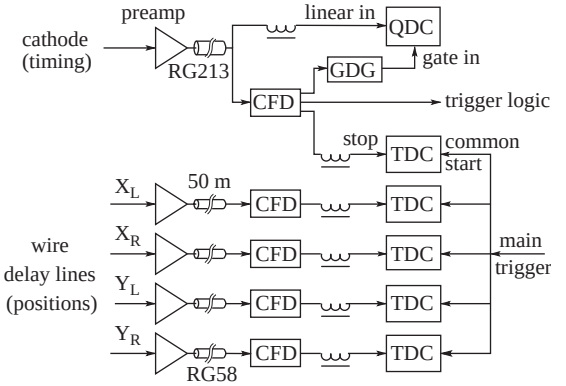

Fig. 11. Schematic drawing of the electronic chain for the PPADs.

different IMFs ($Z = 10, 12, 14$), detected and identified by the phoswiches mounted behind the PPAD. For all IMFs, the efficiency of 50% corresponds to an estimated energy loss in the gas of $\sim$18–22 keV.

3.1.2. The electronic chain

A schematic diagram of the electronics for the PPADs is shown in Fig. 11. Each detector delivers five signals, i.e. one signal from the cathode (“timing” signal) and four “position” signals from the left and right ends of the two “x” and “y” delay lines (X_L, X_R and Y_L, Y_R). Each signal is processed by a voltage-sensitive preamplifier, directly mounted on the frame of the PPAD.

The main characteristic of the cathode preamplifiers, specifically developed in our electronic workshop, are: rise time $\approx$5 ns, decay time $\approx$30 ns and gain $\approx$70. In order to mitigate the effect of different shapes for signals traveling different lengths of the delay lines and to homogenize the response of the following Constant Fraction Discriminator (CFD), slower preamplifiers (model FL8000 developed in GSI, Darmstadt [16]) are used for the position signals (rise time $\approx$12 ns, decay time $\approx$40 ns and gain $\approx$30).

After the preamplifier, the timing signal travels along a $\sim$50 m long RG213 cable connecting the experimental cave with the acquisition room and then enters into a 50 Ω two-way symmetric splitter; one of the split signals is sent to a Charge to Digital Converter (QDC, CAEN model VN1485AS; 4096 channels, full scale 1.3 nC) for measuring the ionization produced in the detector. The other split signal is sent to a CFD with a delay of 2.5 ns and a fraction of 0.3 (CAEN model C671). Its prompt output is sent to a Gate & Delay Generator (GDG), which produces the integration gate for the QDC, and—with signals of other detectors—to the trigger logic, which generates the main trigger (see Section 4). All the GDGs have been developed and built in our electronic workshop. The CFD delayed output (delay of about 400 ns) gives the stop to a Time to Digital Converter (TDC, CAEN model VN1488AS; full scale 400 ns), whose start is the above mentioned main trigger of the experiment.

The four position signals from the delay line preamplifiers travel along $\sim$50 m long RG58 cables and are then processed by four CFDs (CAEN model C671; delay 20 ns and fraction 0.5), the delayed outputs giving the stop to four TDCs (CAEN model VN1488AS; full scale 800 ns), whose common start is the main trigger.

3.1.3. Calibrations and performances

The calibration procedure consists of the following steps:

(1) channel-to-ns conversion of all TDC channels;
(2) for the time-of-flight determination:
- correction of the dependence of the time signal on the impact point on the detector (see Fig. 9).

- determination of the absolute offset of a reference detector (e.g. PPAD #1), which is below the grazing angle of the PLF for all the studied reactions;
- determination of the relative offsets of all the other detectors with respect to the reference one;

(3) for the position signals: conversion from ns to mm.

Concerning point (1), during the production runs the start and stop signals of a Time Calibrator (EG&G ORTEC model 462) are sent to all the TDCs, in order to check their stability and calibrate their scale. The repetition rate is typically 0.2 Hz and the stop signals are randomly spaced by multiples of the period of 20 ns, in a range of 1.2 μs. The Time Calibrator stability is better than 10 ppm/°C and the accuracy on the time-distance from pulse to pulse is ±0.005% of the range. A linear calibration of each TDC gives the channel-to-ns conversion, with an integral linearity better than 0.075% of the full scale value. An example of the TDC stability during the second campaign is presented in Fig. 12; the change in the slope coefficient is smaller than 0.2%. Results of similar quality are obtained for all TDCs.

As far as point (2) is concerned, a signal synchronous with the operating radio-frequency (RF) of the Cyclotron can be used for time reference (for the present reactions its period was about 140 ns). For each event, one RF pulse is selected to stop a TDC (started as usual by the main trigger), which thus measures the time relationship between the main trigger and the arrival of a beam pulse on the target (apart from a constant relating the phase of the RF signal to the beam). The subtraction of this TDC conversion (after channel-to-ns calibration) from the calibrated conversions of all other TDCs gives the time of flight of each detected fragment, apart from an unknown offset. For the reference detector this offset is, by definition, the above mentioned "absolute offset" (dependent on the tuning of the Cyclotron), while for all other detectors it consists of the "absolute offset" plus an additional "relative offset" (specific of each detector), which takes into account the difference in the delay of the whole electronic chain of the *i*th detector with respect to the reference one.

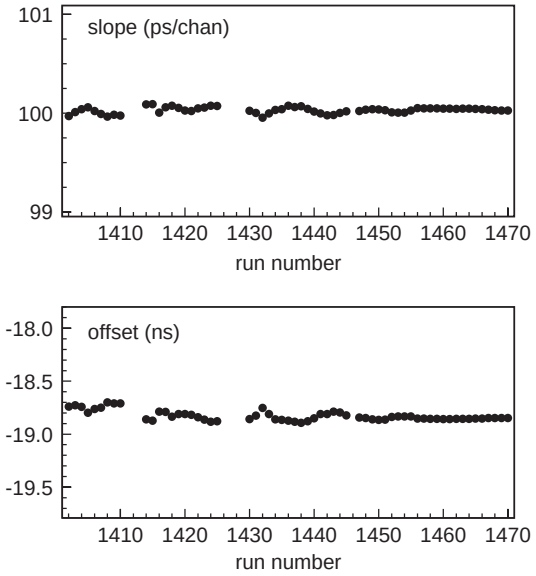

Fig. 12. Trend of the slope (upper part) and offset (lower part) coefficients in the linear calibration of a TDC, as a function of the run number; the displayed data refer to a time period of one week.

Having chosen a reference detector, one can determine the "absolute offset" by imposing that elastically scattered projectiles have the time of flight which can be easily computed from the scattering angle via two-body kinematics; this offset may change in time, due to small changes in the phase relationship between the beam pulses and the RF signal and needs to be determined for each run. The "relative offset" of all the other detectors is obtained, once and for all, from a dedicated measurement at sufficiently low energy so that almost all the PPADs are hit by the coincident products of the elastic scattering: for example, in the first campaign we used the reactions $^{93}Nb + {}^{93}Nb, {}^{197}Au$ with a 7.5 AMeV beam delivered by the Superconducting Cyclotron, while in the second campaign we used $^{28}Si + {}^{58}Ni, {}^{197}Au$ with a 5 AMeV beam from the Tandem and $^{93}Nb + {}^{93}Nb$ at 17 AMeV from the Cyclotron. These low energy reactions have been used also for the already mentioned correction of

the dependence of the time signal on the impact point on the gas detectors.

For the calibration of the position signals, spectra were first obtained by building the difference $X_L - X_R$ for the "x" coordinate and $Y_L - Y_R$ for the "y" coordinate. In the first campaign the ns-to-mm conversion was then obtained simply by "counting the group of wires" (whenever the resolution and the statistics made it possible) or by associating the width of the spectra to the known linear dimensions of 300 mm for the *Quadro*s and 200 mm for the *Punto*s. In the second campaign the calibration of the position signals was improved by mounting a mask of known geometry in front of each PPAD during the low energy runs. An example of the obtained position spectra with the mask superimposed is presented in Fig. 13 for the "x" coordinate of PPAD #2.

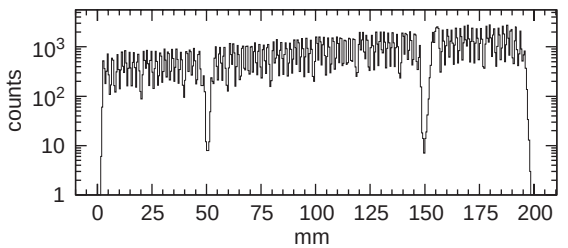

Fig. 13. x-coordinate spectrum from elastic scattering into PPAD#2: one recognizes the peaks corresponding to the different groups of wires, while the two dips at 50 and 150 mm are due to the calibration mask.

As an example of the PPAD's performance, Fig. 14 shows, in a polar representation similar to that of Fig. 5, the experimental yield of two body-events collected by the PPADs for the $^{116}Sn + ^{93}Nb$ reactions at 29.5 AMeV in the first campaign. The forward–backward enhancement is due to the coincident detection of the two reaction partners in elastic and quasi-elastic events.

3.2. The silicon telescopes

The 96 silicon telescopes consist of a 200 μm-thick transmission ΔE detector (uniformity within ± 2 μm), manufactured by *Canberra*, followed by a 500 μm-thick E detector, manufactured by *Hamamatsu*. Both are n-type silicon detectors, with a p^{++} ion-implanted entrance junction and an active area of 30×30 mm^2. To prevent possible edge effects (due to distortions of the electric field) 3 mm-thick brass diaphragms reduce the effective active area to 28×28 mm^2. The silicon chips have been polarized with about 60 V in case of the ΔE detectors (over-bias of $\approx 20\%$ in the first campaign and of a factor of 3–4 in the second one) and with about 130 V in case of the E detectors (overbias of $\approx 30\%$). By constantly monitoring the reverse current, one can estimate the ohmic drop on the bias resistor (11MΩ) and hence the actual voltage across each detector, and compensate for possible variations by adjusting the applied voltage.

Both ΔE and E detectors measure the energy deposited by the incoming particles, while the

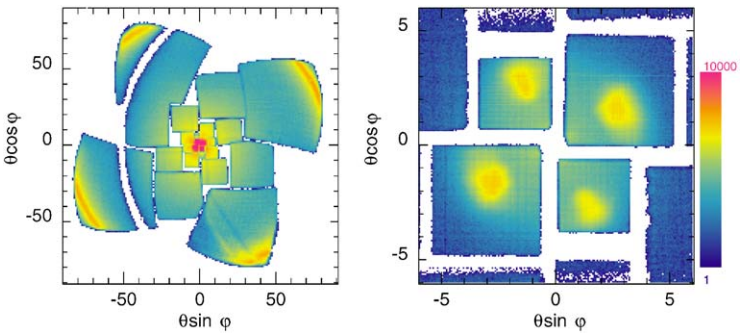

Fig. 14. Polar representation of the experimental two-body yield as measured by the PPADs for the $^{116}Sn + ^{93}Nb$ reaction at 29.5 AMeV in the first campaign. Left side: total view of the forward hemisphere (the circular shadow on the two leftmost detectors is due to the target frame, which was tilted by about 50°). Right side: detail of the first four detectors (the intensified regions are due to coincidences with the four most backward detectors).

Table 2
Bulk resistivity, cutting angle with respect to the {111} crystallographic plane, capacitance, thickness of the dead layers on the front and back side, depletion voltage for the silicon detectors

		Bulk resistivity (Ωcm)	Cut. angle (deg)	Capacit. (pf)	Dead layer (front)		Dead layer (back)		Depl. (V.)
					(μm)	(mg/cm^2)	(μm)	(mg/cm^2)	(V)
ΔE	(a)	2000–5000	7	550	0.18	0.042	0.6	0.14	~50
	(b)	9300–15000	7	550	0.18	0.042	1.1	0.25	15–20
E		5000–12000	0	220	0.40	0.093	~12	~2.8	~100

(a) first campaign; (b) second campaign.

timing information is derived only by the ΔE section. During the first campaign, ΔE detectors with a very thin (≈ 50 nm) entrance metallic layer were used, but the consequent non-negligible surface resistivity of the electrode introduced a dependence of the signal rise time on the impact point (up to 5 ns spread): this caused a deterioration of the time of flight information. To improve the timing, in the second campaign ΔE detectors with a thicker (≈ 100 nm) metallization (and hence a lower surface resistivity) were used. The dead-layer thickness at the front and back side of the ΔE detectors and at the front of the E detectors have been measured in our laboratory with 5.5 MeV α-particles. The obtained values are reported in Table 2, together with other parameters supplied by the manufacturers, like the bulk resistivity, the capacitance, the cutting angle with respect to the {111} crystallographic plane and the thickness of the rear dead layer of the E detectors.

Since, for the moment, pulse shape analysis is not implemented, particles can be identified in charge Z only if they reach the second silicon detector. This requirement determines the low-energy threshold for the Z identification, which, for a 200 μm thick ΔE detector, is estimated to be about 15–20 AMeV for $Z \geqslant 20$. The high-energy limit for the Z identification is determined by the requirement that the particles are stopped in the second silicon detector. The punch-through energy corresponding to the total thickness of one telescope increases with atomic number from ≈ 11 AMeV for $Z = 3$ to ≈ 35 AMeV for $Z = 20$. It further increases for larger Z values, but at all bombarding energies studied up to now with our setup, the telescope thickness was sufficient to stop all the fragments with $Z \geqslant 20$.

Lighter fragments are stopped (and hence identified from the telescope information) only if their energy is low. For more energetic fragments punching through the silicon telescopes, the charge Z can be obtained with the help of the CsI(Tl) scintillators mounted behind. In both cases, the dynamic range of the energy measurement in the silicon detectors needs to be extended (toward the low-energy region), as the deposited energy strongly decreases with increasing energy and decreasing charge Z of the fragments. Therefore in the second campaign the shapers have been provided with a second independent high-gain branch, which allows to push the particle identification with the ΔE–E method down to $Z = 2$. Even more important, this extension of the dynamic range makes it possible to perform a more reliable energy calibration with the help of the low energy beams (Tandem energies).

Mass identification can be obtained from the energy deposited in the telescope and the time of flight measured either by the silicon detector itself or by the coincident PPAD signal. The resolution is of the order of 3% (FWHM), the main contribution being that of the time-of-flight measurement. The so obtained mass identification may also be affected by a systematic error of $\leqslant 1\%$, due to the uncertainty in the pulse height defect (PHD) estimate.

3.2.1. The electronic chain

The electronic chain used for the signals of the silicon telescopes is schematically sketched in Fig. 15. The signals of the silicon detectors are

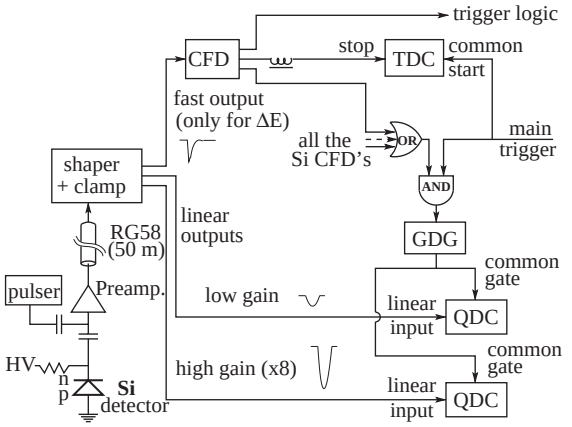

Fig. 15. Schematic diagram of the electronic chain for the silicon detectors.

processed by fast charge-sensitive preamplifiers with low power consumption (about 80 mW each), which have been designed and built in our laboratory [17]. They are directly mounted (without any cooling) on the supporting frames of the detectors inside the vacuum scattering chamber. Their main parameters are: rise time $\tau_r \approx 10$ ns, decay time $\tau_d \approx 60$ μs, sensitivity of 2 and 1 mV/MeV for the ΔE and E detectors, respectively.

The output of each preamplifier travels along a 50 m long RG58 cable to the acquisition room, where it is fed to a shaper, featuring one fast output and two linear outputs with different gains (only one linear output in the first campaign). The fast output is obtained by differentiating ($\tau = 100$ ns) the input, with high amplification and with a clipping circuit to avoid long recovery times associated with the large signals overload. This fast output is actually used only for the ΔE detectors: the signal is then fed to a CFD with a delay of 2.5 ns and fraction 0.3 (CAEN model C671). The delayed CFD output provides the stop signal to a TDC (CAEN model VN1488AS) used in common start mode (start given by the main trigger).

The two linear outputs of each shaper are used for the measurement of the energy deposited in the silicon detector; their gains can be set independently and in our experiments they have been chosen so as to differ by a factor ≈ 8. To produce the linear outputs, the shaper first performs a bipolar shaping (with a peak time of 1 μs) and then selects, with a clamp circuit, the first lobe of the signals; this technique is very similar to that described in Ref. [10]. These linear outputs are integrated by two QDCs (CAEN model VN1475AS, with 4096 channels and full scale 13 nC). The integration gate, common to all silicon detectors, is generated, via a GDG, from a general OR of all the outputs of the silicon CFDs. The gate width is somewhat larger than the time duration of the unipolar clamped output (≈ 2 μs) in order to provide a clean integration of the full signal, in spite of the unavoidable spread in the arrival times of the particles on the detectors.

During the data taking, amplitude-programmable pulsers (built by the *Service d'Électronique et Informatique* of CEA, Saclay), triggered by the same Time Calibrator which provides the calibration of the TDCs, deliver a sequence of pulses of predefined amplitudes, in the range 0–4 V, to the test input of each preamplifier.

This information is then used for correcting possible non-linearities of the whole electronic chain, for determining the channel-to-mV calibration of the QDCs conversions (with respect to the signal amplitude of the pulser) and for a continuous check of the long-term stability of the electronic chain during the measurements. The programmable pulsers have integral non-linearities better than 0.1% and thermal coefficients better than 100 ppm/°C.

3.2.2. Calibrations and performances

The energy calibration has been performed in three steps:

(1) channel-to-mV conversion by means of a linear fit to the pulser peaks
(2) mV-to-MeV conversion by means of low energy reactions (^{12}C beam at 95 MeV in the first campaign and ^{28}Si + ^{58}Ni, ^{197}Au at 85 and 140 MeV in the second one)
(3) definition of a set of identification lines to obtain the atomic number Z of the detected fragment from the ΔE–E correlation; charge identification is then obtained with an interpolation between adjacent lines (a similar

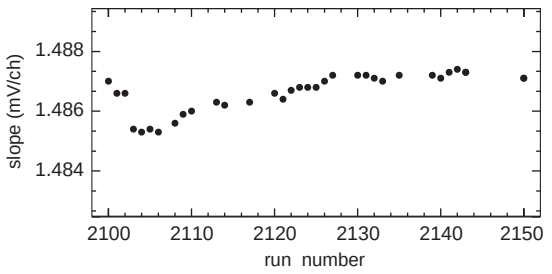

Fig. 16. Variation of the linear coefficient for the calibration channel-to-mV (of the pulser) as a function of the run number (for a time period of one week), for a representative silicon detector.

procedure is used also for the phoswich telescopes).

By means of the pulser peaks collected during the measurements, it has been verified that the overall integral non-linearity of the QDCs (and of the preceding electronics) is better than 0.15%, thus allowing the use of a linear calibration for the channel-to-mV transformation. It was found that the amplification of the electronic chain changes by at most 0.2% in a time period of one week, as can be seen from Fig. 16. The mV-to-MeV conversion has been performed by means of the low-energy elastic scattering of a beam of ^{12}C or ^{28}Si, under the assumption that for such light nuclei the Pulse Height Defect (PHD) is negligible.

An example of a ΔE–E correlation obtained for one telescope in the reaction $^{116}Sn + ^{93}Nb$ at 29.5 AMeV (first campaign) is presented in Fig. 17. The lines show the identification grid which has been obtained [18] from energy loss calculations based on the tables of Hubert [19], using for each element the mass value predicted by the so-called EPAX formula [20] and the PHD estimate obtained from the formula proposed by Ogihara [21]. The so obtained Z identification is presented in Fig. 18, for the $Z = 10$–50 range.[4]

One evident feature of Fig. 17 is that the yield of the elastically scattered ions is distributed along a line with slope ≈ -1. This is attributed to a "channeling" effect of the incoming ion in the transmission ΔE detector. In fact, particles impinging along privileged directions (crystallographic axes or planes) get "channeled", at least for part of their path, thus traveling at a larger average distance from the atoms of the medium than in case of random incidence (see e.g. Ref. [22] for a study of channeling of heavy ions in the

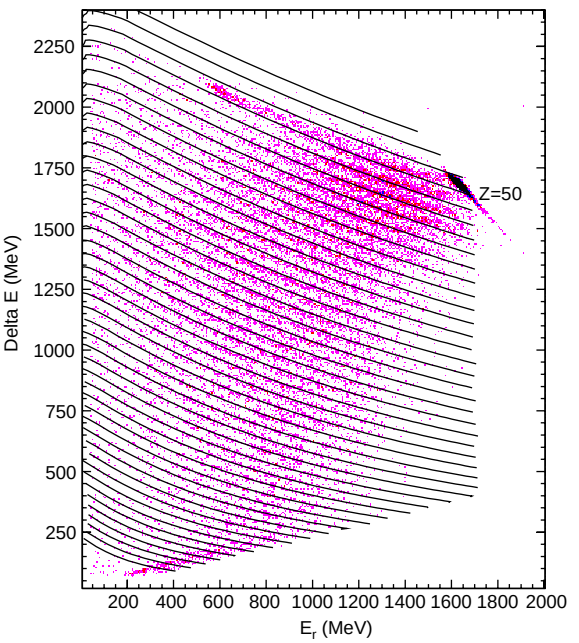

Fig. 17. ΔE–E_r correlation for one typical telescope in the reaction $^{116}Sn + ^{93}Nb$ at 29.5 AMeV. The lines are those used for Z-identification. The intensification along the line $Z = 50$, at $E \approx 600$ MeV, is due to elastic projectiles slowed down by the passage through the grid wires of the PPAD [12].

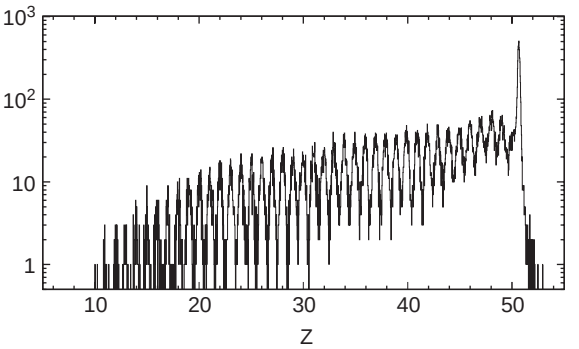

Fig. 18. A typical charge spectrum obtained with a silicon telescope in the first campaign.

[4] The EPAX formula gives for Sn a mass lower than that of the projectile, $A = 116$, therefore in the quasi-elastic region the Z-identification is slightly overestimated, as shown by the value $Z \approx 50.5$ for Sn.

Table 3
Some properties of the scintillator materials used for the phoswich detectors

	Rise time (ns)	Decay time (ns)	Wavelength at max. (nm)	Light yield (photons/MeV)	Density (g/cm^3)	Refract. index	Softening temp. (°C)
BC404	0.7	1.8	408	~12000	1.03	1.58	70
BC444	19.5	180	428	~7000	1.03	1.58	70
CsI(Tl)	~20	600–3500	550	~52000	4.51	1.79	—

Fermi energy regime). Therefore, particles channeled in the ΔE detector undergo a reduced energy loss, but deposit a correspondingly larger amount of energy in the following E detector. Of course, channeling phenomena happen for all ions, resulting in an overall worsening of the charge resolution of the telescopes, although their effect is clearly visible only for the elastic peak, because of its very large statistics.

3.3. The phoswich telescopes

3.3.1. Description

The detection of light charged particles (LCP) and intermediate mass fragments (IMF) is accomplished with arrays of phoswiches, placed behind most PPADs. They are scintillation detectors made of two or three different scintillation layers (all read out by a single photomultiplier), which have been developed and assembled in our laboratory. During the first campaign, both two- and three-layer phoswiches were mounted; in the second campaign only triple phoswiches have been employed, plus a few simple CsI(Tl) scintillators at the very forward angles behind the silicon telescopes. All phoswiches have an active area of 64 × 64 mm^2. The double phoswiches consist of a thin layer (about 200 μm) of fast plastic scintillator (BICRON BC404, bulk material polyvinyltoluene, decay constant $\tau = 1.8$ ns) followed by a 3 (or 5) cm thick CsI(Tl) crystal. In the triple phoswiches a 5 mm-thick slow plastic scintillator (BICRON BC444, bulk material polyvinyltoluene, decay constant $\tau = 180$ ns) is mounted between a 150 μm thin BC404 and the CsI(Tl). Some properties of the three scintillator materials are given in Table 3. A sketch of the telescopes is presented in Fig. 19.

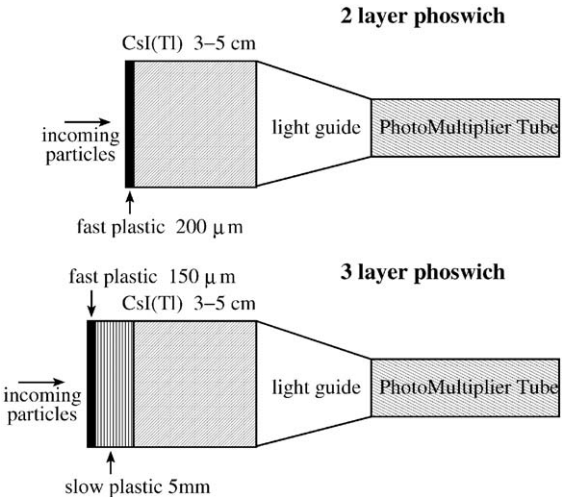

Fig. 19. Sketch of a double (upper part) and a triple (lower part) phoswich telescope.

The threshold for particle identification is determined by the thickness of the first, fast plastic layer. Its average thickness was around 200 μm in the first campaign (corresponding to a threshold of about 3.5 AMeV for LCPs and IMFs), while in the second campaign, where bombarding energies as low as 17 AMeV have been studied, the average thickness has been reduced to about 150 μm (with a threshold of ≈3 AMeV). Basing on simulations [23], it is estimated that, in order to obtain a sufficient resolution for charge identification of IMFs, the thickness inhomogeneity of the first scintillator layer must be not worse than about 5%. Unfortunately, so thin scintillators with such a good homogeneity are not commercially available. Therefore, the required characteristics were achieved in the machine shop of the Department of Physics in Florence, by accurately milling a thicker material with a procedure purposely

developed for this task (vacuum vise and high-velocity diamond tool).

In the double phoswiches, the fast plastic layer, optically polished, simply rested on the front face of the CsI(Tl) crystal, which—being hygroscopic—was first protected by gluing a thin (8 μm) transparent Mylar foil onto it. In the triple phoswiches, in order to avoid an additional dead layer and to keep the thresholds as low as possible, the fast and the slow plastic scintillators were coupled to each other with the "heat pressing" technique, instead of gluing them together with an optical glue. Another advantage is that the Fresnel losses, due to the mismatch of the refraction index of the glue layer, are nominally absent if the two scintillators, which are both made of the same bulk material, are "heat pressed" against each other.

The heat pressing sequence has been implemented following the procedure outlined in Ref. [24], but with some significant modifications. The slow plastic scintillator is first diamond-milled down to the prescribed thickness of 5 mm. With a lapping–polishing machine, both surfaces are then lapped parallel and flat with a 9 μm alumina powder; one of the two surfaces is finally polished with a 1 μm alumina powder. Both surfaces of the thin scintillator come out from the milling procedure flat and sufficiently finished for the next step. Only samples within the prescribed thickness homogeneity (better than 5%) are used. In a 2 cm deep receptacle of a copper block—which can be heated and kept at a constant temperature (within 0.1°C)—one lays (see Fig. 20) on top of each other: a 6 mm thick optically flat glass plate, the thin fast plastic scintillator, the 5 mm thick slow scintillator (with the lapped surface in contact with the fast scintillator), another 6 mm thick optically flat glass plate and a 7 kg lead weight. The material stack is assembled at room temperature. The copper block and the stack are placed in a vacuum vessel and pumped down, while at the same time the heater is turned on: the temperature increases and outgassing takes place. When the temperature reaches the value of ≈85°C (after about 1 h), the pump is switched off, air is slowly admitted into the vessel and an additional weight of about 6 kg is laid on top of the stack. With further heating, the copper block reaches in few more minutes the final temperature of 94°C and the plastic scintillators are "cooked" for the next 10 h. The heater is then switched off and the stack slowly (in about 10 h) reaches the room temperature.

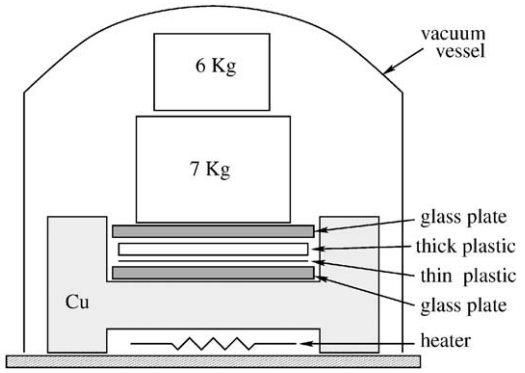

Fig. 20. Sketch of the device used to heat-press the fast and the slow plastic scintillators.

The two plastic scintillators emerge from this operation as an apparently transparent, flat, single scintillator: in fact, the heat-pressing of the front face of the thin scintillator against the flat glass makes it optically flat too. Besides, any residual roughness of the other face of the fast scintillator vanishes when the two scintillators amalgamate at the softening temperature of 94°C. The described protocol was established after many trials. The pump-down procedure is fundamental in order to avoid the trapping of air (or gas) bubbles between the two amalgamating surfaces.

The value of the softening temperature was somewhat critical and differs significantly from what is reported in Ref. [24]. The difference can be ascribed neither to a poor temperature inhomogeneity, nor to a systematic error in the temperature measurement of our setup. In fact the temperature is measured by means of a platinum resistance inserted in the copper block and moreover, by means of four additional sensors placed in different parts of the copper block, it has been verified that its temperature homogeneity is better than 0.1°C. The different scintillators (BC408 in Ref. [24] and BC404 in our case) are unlikely to be responsible for this difference since the bulk material is the same. The difference may rather be ascribed to the fact that in our heat-pressing

setup the complex of the two scintillators is small enough to be totally contained in the copper receptacle. Therefore, with respect to the setup of Ref. [24], the radiant heat losses are expected to be significantly smaller and the measured temperature is presumably closer to the value reached at the interface between the two scintillators.

In the first campaign, the so obtained two-scintillator layer simply rested on the CsI(Tl) front face; in the second campaign it was glued onto the CsI(Tl) crystal, but unfortunately in some cases it detached, thus worsening the overall detector resolution.

The light of the two or three scintillator layers reaches the photomultiplier tube (PMT) through a tapered light guide. The light guide is coupled at one end with the CsI(Tl) and at the other end with the photomultiplier tube via an optical glue. The sides of the scintillator stack and of the light guide are wrapped first with white paper and teflon tape (to improve the diffusion and collection of the fluorescence light) and then with black tape (to shield from external light). A 3 μm-thick aluminized Mylar foil is also stretched on the front face of the fast plastic scintillator in order to partially protect the phoswich from light (in any case during the measurements no light sources are present inside the scattering chamber).

The photomultiplier (EMI model 9954B) is provided with an active voltage divider, developed and tested in our laboratory. Because of its very low power consumption (≈ 0.3 W), it can be operated under vacuum without need for a cooling system. The photocathode is of the bialkali alloy (Rb–Cs) type, optimized for the detection of blue and green light (quantum efficiency of 26% at 400 nm). The nominal dark current is 2 nA, the gain typically 10^6 and the single photoelectron rise time is about 2 ns.

3.3.2. The electronic chain

With reference to Fig. 21, each anode current pulse travels along a ~ 50 m long RG213 cable from the scattering chamber to the acquisition room and is sent to the input of a four-way asymmetric 50 Ω splitter; of the emerging signals, the one with 50% amplitude is fed to the CFD, while the other three (25%, 12.5% and 12.5% of

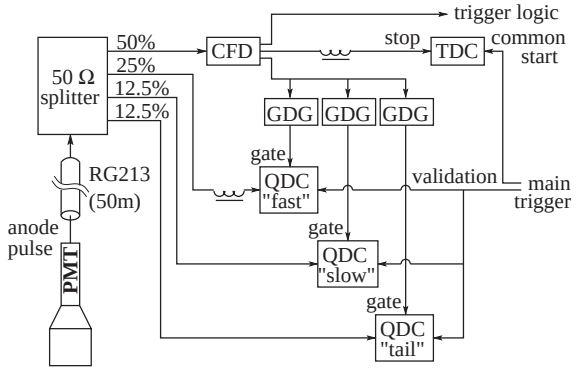

Fig. 21. Schematic diagram of the phoswich electronic chain as assembled during the second campaign.

the original signal) are sent to three QDCs, which are named "*fast*", "*slow*" and "*tail*", as they integrate different parts of the incoming signal (the fast, the slow and the tail component, respectively). All the QDCs have 4096 channels and a full scale of 1.3 nC. A delay of about 80 ns is necessary on the input to the *fast*-QDC in order to allow for the formation of its gate. With one exception, the gates are individually generated (one for each detector) from the prompt outputs of the CFDs and the QDCs (CAEN model VN1485AS) are used in the asynchronous mode, i.e. they perform a free-running integration of the input signal inside the gate, while the digitization is performed only if a validation signal is issued by the main trigger within a preset time interval (less than 1 μs). The exception was the *tail*-QDC in the first campaign (CAEN model VN1475AS), which worked synchronously and had just one common gate for all phoswiches, generated by an AND between the main trigger and the OR of all the phoswich CFD outputs. Finally, in order to measure the time of flight of the detected particles, the delayed output of the CFD stops a TDC (CAEN model VN1488AS), whose start is given by the main trigger.

As sketched in Fig. 22, the gate of the *fast*-QDC (fast gate) begins a few ns before the leading edge of the PMT signal and lasts about 50 ns, thus integrating mainly the signal of the fast plastic. The gate of the *slow*-QDC (slow gate) begins about 200 ns after the end of the fast gate and lasts about 250 ns; it integrates mainly the signal of the slow

plastic (if present) and the fast component of the CsI(Tl). The gate of the *tail*-QDC (tail gate) begins ≈ 1 μs after the end of the slow gate, lasts about 1 μs and it mainly samples the light from the slow component of the CsI(Tl).

To check the stability of the PMT amplification, during operation an optical fiber injects light pulses into each PMT. In order to mimic the shape of the phoswich light production, these pulses are obtained from the fluorescence light emitted by a stack of a CsI(Tl) crystal and a fast plastic scintillator excited by a light pulse of a UV-N_2 laser. Diaphragms of different opening are applied to the laser output in order to get calibration pulses of different amplitudes, while the intensity of the laser pulses is monitored by a silicon photodiode.

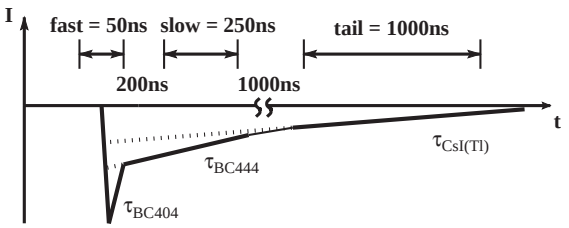

Fig. 22. Sketch of the integration gates for the anode signal of the phoswich telescopes; the time axis is not in scale.

3.3.3. Calibrations and performances

At variance with most other arrays of scintillation detectors, the particle velocity is directly obtained from the measured time-of-flight (together with a good-quality pulsed beam), with no need for lengthy and complicated energy calibrations of the phoswiches, which would require many different beams at different energies. For light charged particles, which can be isotopically resolved, the energy is trivially deduced from their velocity, while for IMFs, which are identified only in atomic charge Z, one needs some assumption about their mass value: the usual assumption is $A = 2Z$.

The channel-to-ns conversion of the TDCs scale is performed by means of the Time Calibrator, in the same way as already described for the PPADs, obtaining similar values of linearity and stability. The offset of the time axis can be obtained with one of the following procedures.

The first one exploits the occurrence of higher-Z fragments with sufficiently large energy to be detected both by a phoswich and by the PPAD in front of it (see Fig. 23): this method cannot be applied to all detectors because at large polar angles too few coincidences phoswich-PPAD are observed. Once the gas detector is independently calibrated by means of elastic scattering (see Section 3.1.3), the time offset of the phoswich is

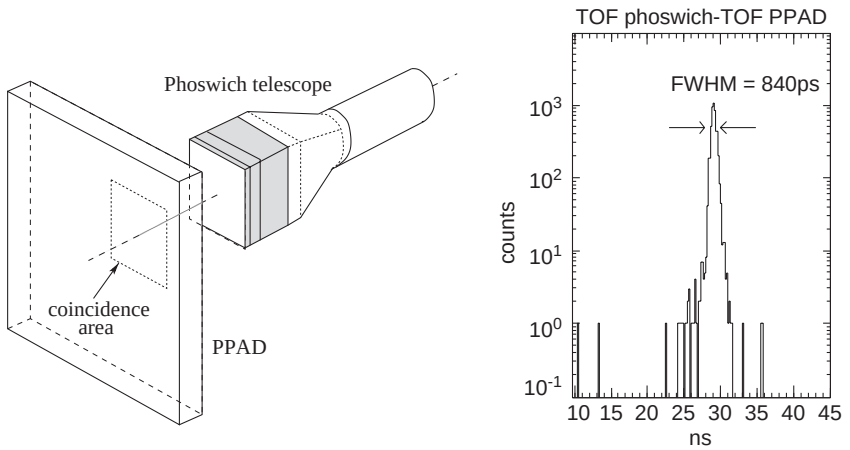

Fig. 23. Left side: the region of the PPAD selected for the detection of high Z particles in coincidence with the phoswich telescope. Right side: an example of the spectrum of the differences between the time-of-flight given by the PPAD and that given by the phoswich, before correcting for the relative offset.

determined in such a way that the difference between the times of flight measured by the two detectors (corrected for the few millimeters of distance between the PPAD and the phoswich) vanishes. An example of the obtained time difference (before offset determination) is presented on the right side of Fig. 23; the width (FWHM) of the obtained distribution is about 840 ps.

In the second procedure the time offset is determined from the protons and α particles punching through the plastic scintillators of known thickness: according to the tables of Janni [25], the punch-through energy of protons for the fast plastic is about 3.5 MeV, while that for the two plastic scintillators together is about 23 MeV.

The FWHM resolution of the time-of-flight measured by the phoswiches is given in both cases by the intrinsic time resolution of the phoswiches (about 700 ps) and of the beam pulses (between 600 ps and 1 ns FWHM). In the first procedure, after combining these values with the uncertainty in the determination of the offset (see right side of Fig. 23), one obtains an overall accuracy on the time-of-flight determination of the order of 1.3–1.5 ns. In the second procedure, when combining the time resolutions with the uncertainties in the determination of the punch-through point from the experimental correlations (which is of the order of 300 ps FWHM) and in the measurement of the scintillator thickness (usually negligible) one obtains a slightly better overall accuracy of about 1.0–1.2 ns; a systematic error may of course result from the possible inaccuracy (5–10%) of the energy-loss tables. After all, the second procedure is preferred, as it can be applied to all phoswiches.

The plots of Fig. 24 show typical examples of experimental correlations *fast–slow* (a,b), *slow–tail* (c,d) and *fast–time-of-flight* (e,f), respectively, from the reaction $^{93}\mathrm{Nb} + {}^{116}\mathrm{Sn}$ at 30 AMeV, for two phoswiches mounted at similar laboratory angles ($\vartheta \approx 12^{\circ}$): the left panels (a,c,e) are for a double phoswich and the right panels (b,d,f) for a triple one. The *fast–slow* correlations (Fig. 24a,b) are used for the element identification of particles with $Z \geqslant 2$ (IMFs and helium); the particles stopped in the fast plastic (nearly vertical ridges in the pictures) cannot be identified and this sets an identification threshold of about 3–3.5 AMeV. In the triple telescope, one can distinguish two main regions: the first one (upper octant) corresponds to particles stopped in the slow plastic, the second one (lower octant) to particles stopped in the CsI(Tl). The change in slope between the two regions is due to the larger scintillation efficiency of the CsI(Tl) with respect to the plastic scintillators. In the lower octant only the contribution associated to LCPs and IMFs with low Z (mainly Li and Be) is present, because the heavier clusters have not enough energy to reach the CsI crystal.

Figs. 24c and d show, for the same double and triple phoswiches, the *slow–tail* correlations which can be used for an isotopic separation of hydrogen nuclei and, to some extent, of ^{3}He and ^{4}He. In the double phoswich this correlation is solely due to the pulse shape discrimination of the CsI(Tl); in the triple phoswich an additional ΔE-like contribution from the slow plastic helps the discrimination of the particles even when they barely enter the CsI(Tl). However, in this latter case, the particles need to have enough energy to punch through both plastic scintillators and for this reason most IMFs are concentrated in the nearly vertical ridge on the left.

The correlations *fast* vs. *time-of-flight* (Fig. 24e, f) give the isotopic separation of less energetic protons, deuterons and tritons: in fact, for particles punching through the fast plastic (corresponding in the figure to times of flight $\lesssim 60$ ns), the *fast* signal gives an estimate of their energy loss. The partial overlap of tritons and α particles, which prevents a correct identification of tritons, is avoided if the same correlation *fast* vs. *time-of-flight* is built under the requirement that the particles are first identified as hydrogen isotopes from the *fast–slow* correlation (Fig. 24a and b), as can be seen in Fig. 25 for the case of a triple phoswich.

The Z-identification grids (an example is shown in Fig. 26) are hand-drawn following the ridges of the correlations, one for each particle species. An individual set of lines is used for each telescope: in fact the detector response depends on a number of non perfectly controlled parameters (like non-linearities, quenching and differences in the photomultiplier and CsI(Tl) response) and the

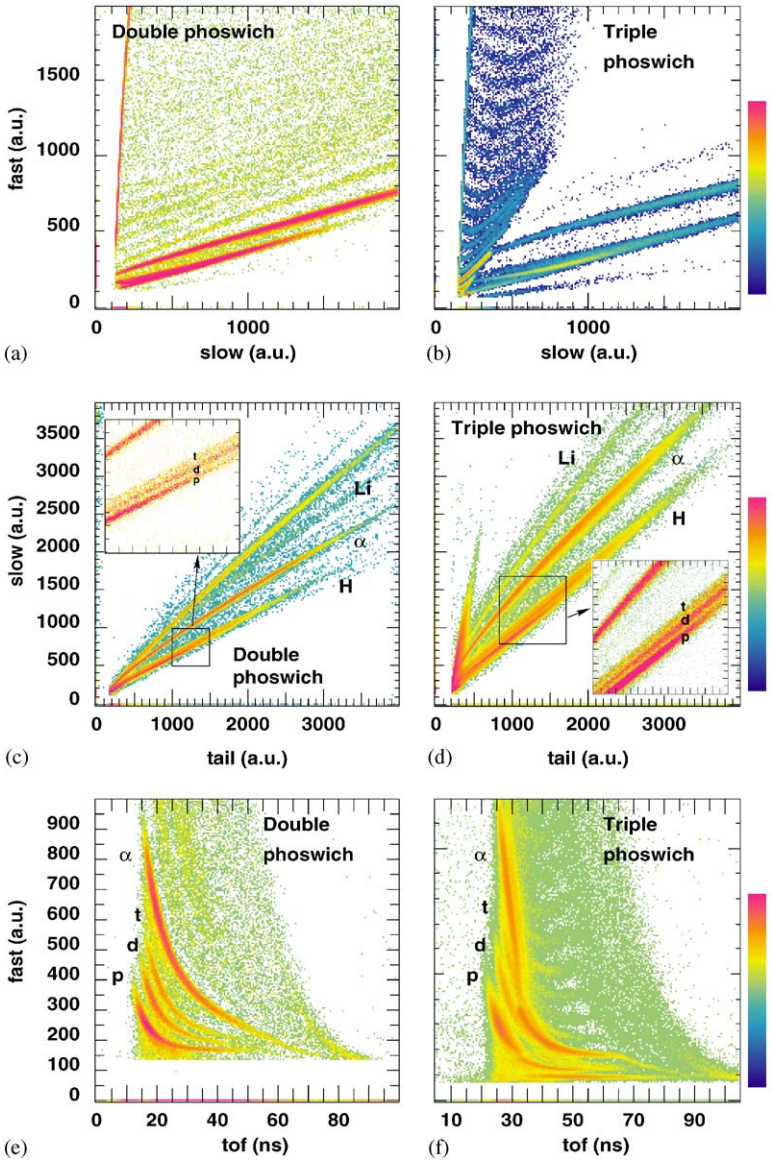

Fig. 24. Experimental correlations for one double (left panels: a,c,e) and one triple phoswich (right panels: b,d,f), i.e the *fast* vs. *slow* correlations (a,b), the *slow* vs. *tail* correlations (c,d) and the *fast* vs. *time-of-flight* (before offset determination) correlations (e,f), respectively.

use of a single grid for several detectors would somewhat spoil the quality of the obtainable identification. Alternative methods, employing neural networks, are under study.

An example of the obtained particle identification is presented in Fig. 27 (particles with low Z) and Fig. 28 (fragments with higher charge), for the phoswiches of Fig. 24. The isotopic resolution for p, d, t is comparable for both kinds of telescopes, while a good element identification of IMFs with relatively high atomic number ($Z \approx 15$–20) is obtained only in the case of the triple phoswiches. This result can be understood considering that, at our energies, most IMFs do not reach the CsI

crystal of the triple phoswiches, but are stopped in the slow plastic. As pointed out in Section 3.3.1, at the junction between the two plastic scintillators the energy losses (due to dead layers) and the light losses (due to refraction index mismatch) are strongly reduced (thanks to the "heat pressing" technique) with respect to those occurring at the junction between plastic scintillator and CsI. Therefore in the second campaign all double phoswiches have been replaced by triple ones. The only exceptions are the scintillators behind the silicon telescopes where simple CsI(Tl) crystals are used, but also in this case it is possible to identify

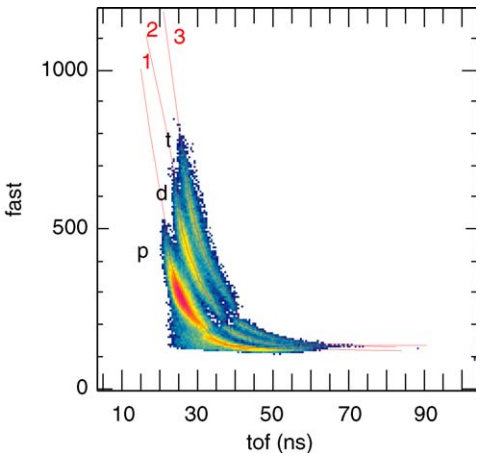

Fig. 25. The *fast* vs. *time-of-flight* correlation for the triple phoswich of Fig. 24f after selecting the hydrogen isotopes via the *fast* vs. *slow* correlation of Fig. 24b (the discontinuities around 30–40 ns are due to the entrance of the particles into the CsI(Tl), which has a larger scintillation efficiency than the plastic scintillators).

energetic light charged particles. Indeed, one can either use the information from both detectors (ΔE(silicon)–E(CsI) correlation), or that from the CsI(Tl) alone: namely one can exploit the pulse shape discrimination or—even better in case of long flight-paths—the *slow* vs. *time-of-flight* correlation (hydrogens and heliums have to be first separated from the *slow–tail* correlation, as done in Fig. 25 for the phoswiches).

3.3.4. The multiple hit estimate

The pile up of the very slow phoswich signals (due to random coincidences corresponding to particles produced in different events) can be controlled by proper selection of the beam current and target thickness. In all measurements, the

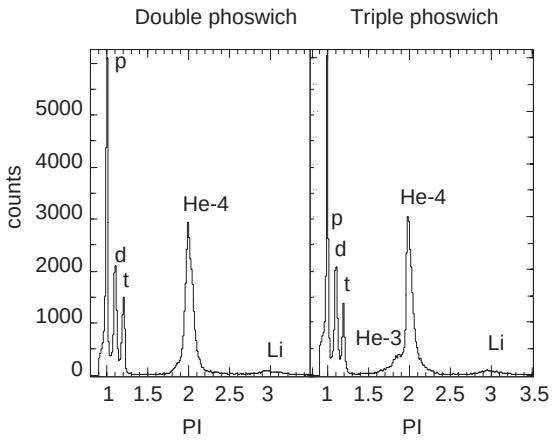

Fig. 27. Particle identification of p, d, t, He and Li in a triple (right side) and double phoswich (left side).

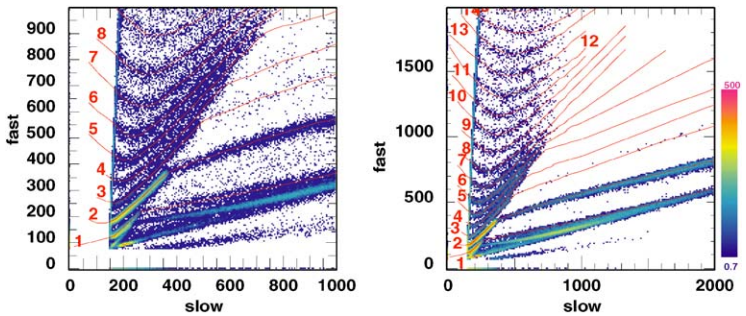

Fig. 26. The *fast* vs. *slow* correlation for the triple phoswich of Fig. 24b, with superimposed the Particle Identification (PI) lines; the labels show the atomic charge associated to each line. On the left side the low energy zone is expanded.

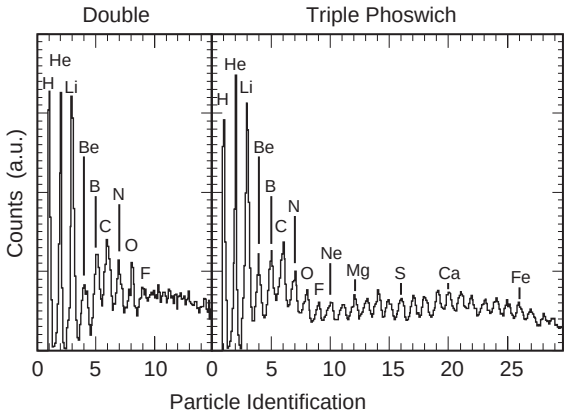

Fig. 28. Particle identification of high-Z particles (here PI $\approx Z$) in a triple (right side) and double phoswich (left side); the yields of H and He are divided by a factor 20.

beam current was kept at a value ($\lesssim$0.8–1.0 nA) such that, with typical target thicknesses of $\approx$200 μg/cm^2, pile up effects can be neglected (probability less than 0.2%).

On the contrary, the double hit probability (due to two—or more—particles produced in the same event impinging on the same detector) does not depend on the beam current and target thickness, but rather on the multiplicity of particles, on their angular distribution and on the detector solid angle. It cannot be neglected, although it is rather small for most phoswiches thanks to the high granularity of the setup over a large portion of the solid angle. Multiple hits are mainly caused by the more abundant LCPs and their importance increases with increasing centrality of the collision. In a double hit event, the recorded time of flight is that associated with the faster particle, while the recorded energy corresponds to the sum of the energies deposited by both particles. In this way an erroneous particle identification is obtained, thus worsening the overall resolution.

A quantitative estimate of this effect can be obtained from the experimental data: the double hit probability has been obtained, as a function of the inelasticity of the collision, from the probability of detecting two particles in two adjacent detectors (a good approximation as long as small angle correlations can be neglected) [6]. For example, for each phoswich, the number of hydrogen particles detected in coincidence with a second hydrogen in an adjacent detector, divided by the total number of detected hydrogens gives an estimate of the percentage of hydrogen–hydrogen multiple hits in the considered phoswich. Similar estimates have been obtained for the other most abundant combinations, namely helium–helium and hydrogen–helium double hits.

The double hit probability is more important for phoswiches belonging to the blocks #10–20, because they are closer to the target and still at quite forward angles (see Table 1). For near-peripheral collisions ($b/b_{\text{grazing}} \approx 0.9$–$0.7$),[5] even in the worst situation (blocks #13 and #15), the estimated percentage of multiple hits is of the order of 1–2% of the total number of detected hydrogen or helium ions, while it grows up to 4–5% for semiperipheral collisions (b/b_{grazing} between 0.6 and 0.4).

In order to understand how the identification procedure misinterprets the double hit events, an event mixing technique has been applied to the experimental data. The fast, slow and tail signals of identified hydrogen (or helium) ions impinging on the same phoswich in two successive events have been added and the standard identification procedure has been applied to these artificial events (the time of flight of the faster particle has been used as ToF signal). As a result, the double hit of two hydrogens can be identified either as a hydrogen or as a helium (depending on the energy of the two hydrogens), the mixing of a helium and a hydrogen gives a particle still identified as a helium and, finally, the mixing of two helium isotopes mimics a particle mostly identified as a Li ion; this represents an unavoidable systematic error to the determination of the experimental multiplicities of IMFs. It is estimated that the contribution of the double hits to the multiplicities of IMFs with $3 \geqslant Z \geqslant 7$ amounts to 10% at most, while it is negligible for LCPs [6].

[5] The impact parameter is estimated by means of the Quantum Molecular Dynamics code CHIMERA ([5,26,27] for more details see Ref. [6]).

4. The trigger signal

The *main trigger* is obtained from different combinations of the fast outputs of the discriminators (CFDs) associated to the various detectors: it may be either the OR of several detectors of the same type, or the occurrence in a majority logic unit of a multiplicity of detectors above a certain value (e.g. events with two or more PPADs fired), or the coincidence between different detectors (e.g. two PPADs and one or more phoswiches).[6] For example, these are the combinations used in the second campaign:

(1) $Q_{\geqslant 1}$: at least one PPAD fired (''singles'');
(2) $Q_{\geqslant 2}$: at least 2 PPADs (''binary events'');
(3) $Q_{\geqslant 3}$: at least 3 PPADs (''3-body events'');
(4) $Si_{\geqslant 1}$: any silicon telescope fired;
(5) $Ph_{\geqslant 1}$: any phoswich or scintillator fired;
(6) $Q_{\geqslant 2}$ AND ($Si_{\geqslant 1}$ OR $Ph_{\geqslant 1}$ OR HODO$_{\geqslant 1}$): a binary reaction with, at least, either a silicon, or a phoswich, or a HODO-CT detector;
(7) *Beam*: the beam-monitor detector fired;
(8) *Calib*: ''pulser'' event for the calibration of TDCs and QDCs.

All these different trigger types (generally occurring with rather different rates) are first fed to a ''trigger box'' (TB8000, developed by GSI, Darmstadt), which provides individually adjustable scale-down factors for each of them: the more inclusive (and usually less interesting) triggers (1, 4 and 5 in the above example) are usually scaled down by large factors while the more exclusive (and potentially more interesting) ones (3, 6) are not reduced. If it survives the scale-down reduction, each trigger-box input sets a bit on a specific bit pattern unit, whose value is recorded for each event, so that in the off-line analysis it is always possible to sort events according to their trigger conditions.

[6] We point out that, since—as illustrated in 3.1.1—the efficiency of the PPADs is very low for LCPs and light IMFs, the number of fired PPADs in each event is expected to directly give the number of heavy fragments emerging from the collision.

The OR of all these scaled-down signals, vetoed by the acquisition *busy* signal, is the main trigger signal. It gives: the interrupt request to the CPUs of the acquisition system, the common start to all the TDCs of the setup, the validation signal to the asynchronous QDCs and the common gate to the other QDCs.

5. The data acquisition

The front-end acquisition ($\sim$1500 input channels) is subdivided into four independent systems operating in parallel, as shown in Fig. 29 (only two were implemented in the first campaign). The TDC and QDC boards are housed in four extended VME (VNX9) crates: each crate contains up to 10 modules and is controlled by a CPU, arbitrating the mastership requests of the local VMEbus and running a stand-alone program which is in charge of collecting the converted data [28]. One of these systems, indicated as *master* in the figure, plays the role of building complete events by merging its own data with those gathered by the *slave* systems in their respective crates: the communications of the data from the *slave* systems is accomplished through *Fast Ethernet* (100 Mbps) point-to-point connections. The *master* system is also connected, through another dedicated *Fast Ethernet* link, to a personal computer (PC) running the Linux operating system. The events, packed into large (some Mbytes) multi-event buffers, are asynchronously dumped to this PC during the intervals between events. The PC stores the buffers on discs and also distributes them, via a *Fast Ethernet LAN* with multicast protocol, to several other PCs for event-by-event on-line analysis of the correlations among the various experimental observables.

The detailed sequence of operations is as follows. During data-taking, the trigger is immediately rearmed once all CPUs have collected—and the *slave* CPUs also transmitted—their data from a previous event; in fact, in order to reduce the overall dead time, the transmitted data are not immediately gathered by the *master* CPU, but remain temporarily stored in the FIFO memory at the receiving end of each *Fast Ethernet* point-to-point connection. When a new event occurs, the

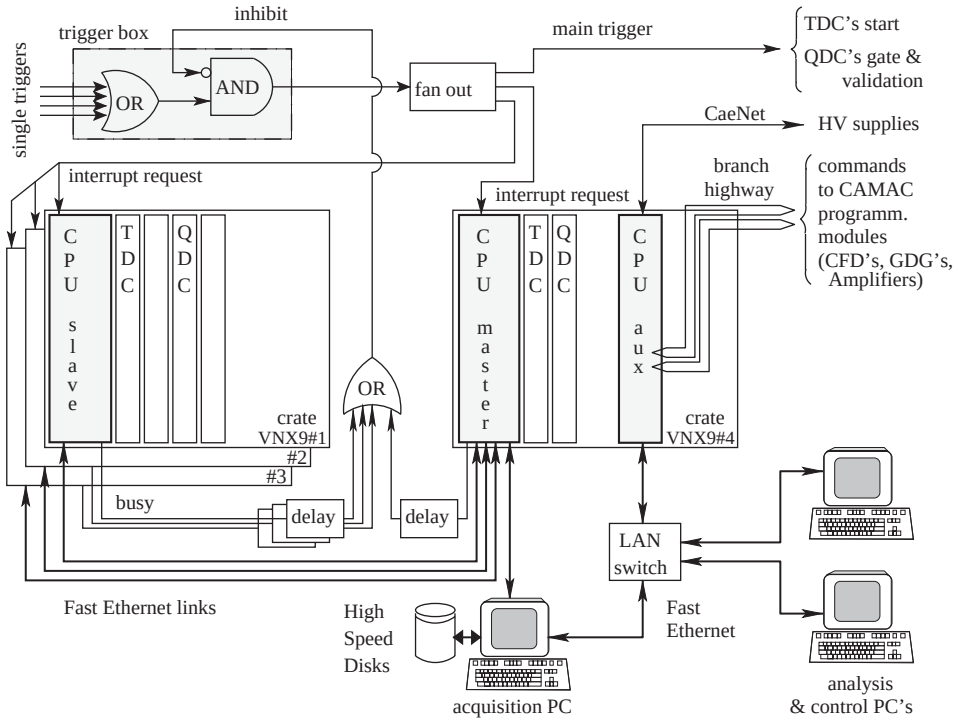

Fig. 29. Schematic diagram of the data acquisition system.

"trigger box" sends an interrupt request to all CPUs and receives back an inhibit signal, with a delay of ~ 300 ns (this allows to latch all possible trigger signals in the bit pattern unit, including those due to slower particles). Moreover, a waiting time of ~ 70 μs begins for all CPUs, while all TDC and QDC boards, in parallel, perform the conversion of all their active inputs (64 inputs are multiplexed on 2 ADCs with a conversion time of ≈ 2 μs for each input). During this waiting period only the *slave* CPUs are idle, the *master* CPU uses part of this time to complete the writing of the previous event, by appending the data already transmitted by the *slave* CPUs (but stored in the FIFO memories) after its own data. After the 70 μs waiting time, each CPU begins to sequentially fetch the converted data of all active channels, writing them into its own memory. Eventually, when all CPUs have completed their task and the *slave* CPUs have sent their data via *Fast Ethernet*, the trigger is rearmed for a new event and the sequence starts again.

A typical acquisition busy-time of ~ 300 μs per event has been measured. The events were acquired at an average rate of 0.2–1.0 kHz (depending on trigger selectivity). The limiting factor was the "singles" count rate which, with the requirement of safe operation with respect to discharges in the PPADs (see Section 3.1.1), determined the maximum allowed beam current.

The *master* crate houses two VME-to-CAMAC Branch HighWay interfaces and a VME-to-CAENet interface, branched to all the detector power supplies (manufactured by CAEN), in order to set and read back the relevant parameters (thresholds and delays of CFDs, amplifier gains, delays of GDGs, voltages of silicons and phototubes): this is performed by a dedicated server program on an auxiliary VME CPU, running Linux. It is therefore possible to record all the experimental settings at the beginning of each run. The server accepts requests via *Fast Ethernet* from clients running on any of the PCs and exploits tasks such as locking a module for access by a client (to avoid conflicts),

queuing accesses to the CAMAC bus and CAENet line, keeping a history of accesses and modifications of the parameters.

During the second campaign the signal of some phoswich and silicon detectors has been also digitized by a 4-channels VME card prototype, with a sampling frequency of 100 M samples/s and 12 bit resolution, employing pipelined ADCs [29]. The particle identification obtained from the digitized signals is comparable (and, in some cases, superior) with respect to that obtained by the standard analogic treatment of the signal; therefore this kind of solution is an effective alternative to traditional methods for future setups, especially if a Digital Signal Processor (DSP) is introduced, able to perform an on-line analysis in order to store on disk only a limited number of parameters necessary for the particle identification [30].

6. Summary and conclusions

The FIASCO multidetector, a setup optimized for peripheral and semi-peripheral heavy ion collisions at Fermi energies, has been described. It consists of Parallel Plate Avalanche Detectors, for the measurement of the velocity vectors of heavy ($Z \gtrsim 10$) fragments, silicon telescopes, for the identification of the charge and the energy of the projectile residues, and scintillation detectors, for the detection of light charged particles ($Z = 1, 2$) and intermediate mass fragments ($3 \leqslant Z \lesssim 20$). The angular coverage (about 70% of the forward hemisphere) of the PPADs and especially the low threshold for the target-like fragment detection (which is the distinctive feature of this apparatus) allow for a good event reconstruction, in particular for semiperipheral and peripheral reactions. Moreover, since the reactions are strongly focused in the forward direction, even the small solid angle covered by the silicon telescopes (ϑ between 1° and 7°) is able to give a good characterization of the projectile residue. Finally, the phoswich telescopes are distributed at various polar angles and cover an important fraction (about 25–30%) of the forward solid angle. In this way it is possible to have both a very accurate reconstruction of the main event and a good sampling of the particle emission pattern.

As a final remark, it has to be noted that the high intrinsic resolution of the PPADs (about 700 ps for the elastic peak), which is fundamental to obtain a good kinematic reconstruction of the event, requires a good quality pulsed beam (FWHM smaller than 1 ns); the crew of the Superconducting Cyclotron of LNS was indeed able to provide us with a beam of such a quality at all the used energies.

Acknowledgements

We wish to thank S. Salamone of the LNS for his continuous support to the experiment. We are grateful to many colleagues of the technical staff of the Department of Physics and INFN Section of Florence. In particular we wish to thank R. Ciaranfi and M. Montecchi for the development of dedicated electronics. Special thanks are due to M. Falorsi, A. Catelani, M. Merciai and N. Pasqualetti for their accurate manufacturing of mechanical parts and for the careful and precise milling of very thin and highly homogeneous layers of the fast plastic scintillator BC404 for the phoswich detectors. We thank also P. Calonaci, D. Lolli, F. Maletta, G. Tobia and F. Velatini for their support in various phases of the setup construction.

References

[1] R.J. Charity, et al., Zeit. Phys. A 341 (1991) 53.
[2] J. Tõke, et al., Phys. Rev. Lett. 75 (1995) 2920.
[3] J.F. Dempsey, et al., Phys. Rev. C 54 (1996) 1710.
[4] J. Łukasik, et al., Phys. Rev. C 55 (1997) 1906.
[5] E. Plagnol, et al., Phys. Rev. C 61 (1999) 014606.
[6] S. Piantelli, Ph.D. Thesis, Firenze (2000).
[7] S. Piantelli, et al., Phys. Rev. Lett. 88 (2002) 052701.
[8] P.M. Milazzo, et al., Nucl. Phys. A 703 (2002) 466.
[9] G. Casini, et al., Nucl. Instr. and Meth. A 277 (1989) 445.
[10] J. Pouthas, et al., Nucl. Instr. and Meth. A 357 (1995) 418.
[11] G. Casini, et al., Phys. Rev. Lett. 78 (1997) 828.
[12] G. Casini, et al., Eur. Phys. Jour. A 9 (2000) 491.
[13] G. Immè et al., Proceeding of the Workshop on Detector and Instrumentation, Acireale, Catania, March 1993.

[14] H. Stelzer, H.W. Daues, N. Shenhav, GSI Scientific Report 1984, GSI85-1.
[15] G.F. Knoll, Radiation Detection and Measurement, 2nd Edition. Wiley, New York, 1989, p. 191.
[16] Delivered by the firm "Physikalische Nachweisgeräte", 64409 Messel, Germany.
[17] N. Taccetti, et al., Nucl. Instr. and Meth. A 496 (2003) 481.
[18] S. Poggi, Laurea Thesis, Firenze, 2000, unpublished.
[19] F. Hubert et al., Atomic Data and Nuclear Data Tables, Vol. 46, 1990, p. 1.
[20] K. Sümmerer, et al., Phys. Rev. C 42 (1990) 2546.
[21] M. Ogihara, et al., Nucl. Instr. and Meth. A 251 (1990) 313.
[22] G. Poggi, et al., Nucl. Instr. and Meth. B 119 (1996) 375.
[23] L. Bidini, Laurea Thesis, Firenze, 2000, unpublished.
[24] C.A. Pruneau, et al., Nucl. Instr. and Meth. A 297 (1990) 404.
[25] J.F. Janni, Atomic Data and Nuclear Data Tables, Academic Press, New York, 1982.
[26] J. Łukasik, et al., Act. Phys. Pol. B 24 (1993) 1959.
[27] J. Łukasik, et al., Phys. Lett. B 318 (1993) 419.
[28] M. Bini, G. Pasquali, to be published.
[29] L. Bardelli, et al., Nucl. Instr. and Meth. A 491 (2002) 244.
[30] F. Giannelli, Laurea Thesis, Firenze, 2001, unpublished.